

RESEARCH ARTICLE

10.1002/2015JB012179

Key Points:

- A modified discrete model is used to model brittle-ductile transition
- Microcracking may increase couple stress
- Couple stress is an indicator for the b-to-d transition

Correspondence to:

W. Sun,
wsun@columbia.edu

Citation:

Zheng, Z., W. Sun, and J. Fish (2016), Micropolar effect on the cataclastic flow and brittle-ductile transition in high-porosity rocks, *J. Geophys. Res. Solid Earth*, 121, doi:10.1002/2015JB012179.

Received 5 MAY 2015

Accepted 7 FEB 2016

Accepted article online 9 FEB 2016

Micropolar effect on the cataclastic flow and brittle-ductile transition in high-porosity rocks

Zheyuan Zheng^{1,2}, WaiChing Sun², and Jacob Fish²

¹Jiangsu Key Laboratory of Engineering Mechanics, Department of Engineering Mechanics, Southeast University, Nanjing, China, ²Department of Civil Engineering and Engineering Mechanics, Fu Foundation School of Engineering and Applied Science, Columbia University, New York, New York, USA

Abstract A micromechanical distinct element method (DEM) model is adopted to analyze the grain-scale mechanism that leads to the brittle-ductile transition in cohesive-frictional materials. The cohesive-frictional materials are idealized as particulate assemblies of circular disks. While the frictional sliding of disks is sensitive to the normal compressive stress exerted on contacts, normal force can be both caused by interpenetration and long-range cohesive bonding between two particles. Our numerical simulations indicate that the proposed DEM model is able to replicate the gradual shift of porosity change from dilation to compaction and failure pattern from localized failures to cataclastic flow upon rising confining pressure in 2-D biaxial tests. More importantly, the micropolar effect is examined by tracking couple stress and microcrack initiation to interpret the transition mechanism. Numerical results indicate that the first invariant of the couple stress remains small for specimen sheared under low confining pressure but increases rapidly when subjected to higher confining pressure. The micropolar responses inferred from DEM simulations reveal that microcracking may occur in a more diffuse and stable manner when the first invariant of the macroscopic couple stress are of higher magnitudes.

1. Introduction

The transition from the brittle to ductile field is of considerable importance in geophysics, geomechanics, and geotechnical engineering applications. It plays a central role in the mechanics of earthquake, the related seismic and ground motion [Smith and Bruhn, 1984; Wong and Baud, 2012], and reservoir mechanics [Nygård et al., 2006]. The brittle-ductile transition that occurs in geological materials is known to be greatly influenced by the temperature, confining pressure, strain rate, and the presence of pore fluid. In this study, our focus is on the behaviors of the dry high-porosity rock in a low-temperature environment. In other words, the rate dependency stemming from diffusion, nonlinear creep, and recrystallization is not considered [Horii and Nemat-Nasser, 1986; Evans et al., 1990]. Instead, this study analyzes the brittle-ductile transition in the low-temperature, rate-independent regime. In this low-temperature, rate-independent regime, the dominant factor that leads to brittle-to-ductile transition is the change of confining pressure [Tullis and Yund, 1980; Paterson and Wong, 2005].

Previous experimental work such as Mogi [1966], Wong et al. [1997, 2004], Paterson and Wong [2005], and Zhu et al. [2010] have established that sandstone may form deformation band, splitting, and cracks when subjected to triaxial loading at low confining pressure, while exhibiting significantly more ductility at higher confining pressure where cataclastic flow may occur. Here we refer to the term cataclastic flow as the macroscopic ductile flow that stemmed from individual grain fracture and slide relative to one another to accommodate changes in geometrical attributes. The formation of deformation bands have been studied via the bifurcation theory [Rudnicki and Rice, 1975; Issen and Rudnicki, 2000; Borja and Aydin, 2004]. These studies established a condition under which nonhomogeneous deformation modes may form as a result of a singular acoustic tensor. The concept of bifurcation analysis has been extended in Borja [2007] in which the author relates the onset of cataclastic flow with the singularity of the fourth-order tangential constitutive tensor [Sun, 2013].

Nevertheless, the micromechanical mechanism that governs the onset and evolution of cataclastic flow is not completely understood or settled, despite some experimental evidence that relates the onset of cataclastic flow with grain size distribution [e.g., Cheung et al., 2012] and mineral composition [e.g., Baud et al., 2015].

This lack of insight from microscale mechanism is partially attributed to the fact that macroscopic bifurcation theory and specimen-scale observations alone are insufficient to provide sufficient micromechanical information to explain the interplay among different mechanisms (e.g., grain crushing, rearrangements, and pore collapses) that lead to the porosity changes of the specimen [Mogi, 1966; Wong *et al.*, 1997; Schöpfer *et al.*, 2013; Sun *et al.*, 2013; Liu *et al.*, 2015].

While discrete or distinct element method (DEM) has been used to study granular materials [e.g., Cundall and Strack, 1979; Oda and Iwashita, 2000; Kuhn *et al.*, 2015] and fractures in the brittle field [D'Addetta *et al.*, 2002; Delenne *et al.*, 2004; Kazerani and Zhao, 2010], the brittle-to-ductile transition has rarely been replicated and analyzed with a single computational model except a few exceptions. For instance, Camones *et al.* [2013] and Zhang and Wong [2013] employ a simple approach to replicate the fragmentation of cemented or bonded assembles in which they argue that tensile strength of the assemblies is stemmed from the bonding between each grain pair. When a fracture criteria is met at the grain contact, the interparticle bond breaks and the fragmented grains may exhibit a pressure-sensitive frictional response similar to those of granular materials. This technique allows one to simulate the pore collapse triggered by grain rearrangement. Alternatively, Wang *et al.* [2008] and Marketos and Bolton [2009] introduced numerical methods to model the compaction bands due to fragmentation of particles. In Wang *et al.* [2008], an artificial particle shrinkage algorithm is introduced to replicate the grain rearrangement triggered by grain fragmentation, whereas Marketos and Bolton [2009] remove the crushed particles or replace them with packing of smaller particles when a fracture criterion is met. These ideas are different from the previous approaches in the sense that the fracture criterion is applied not on the contacts of the grain pairs but on the grains themselves. In particular, Wang *et al.* [2008] have successfully replicated the brittle-ductile transition phenomenon and the shift of failure mode from dilatancy to shear-enhanced compaction under increasing confining pressure. In both cases, the discrete element method is used as a simulation tool and a mean to obtain first-order constitutive responses such as the homogenized Cauchy stress and porosity of the entire specimen. Nevertheless, the high-order constitutive responses, which are closely related to cavities, cracks, and fractures, have rarely been utilized to study brittle-to-ductile transition.

The objective of this research is to analyze the relationship between micropolar behavior and brittle-ductile transition with increasing confining pressure in frictional-cohesive materials with DEM. By tracking the evolution and distribution of couple stress of microcracks in DEM assemblies, we study how micropolar behavior evolves at different confining pressure and determine how couple stress changes in the transition regime. This study also focuses on ductile field that cataclastic flow dominates the failure mode. Tensile bond and rolling resistance are considered in particle interaction; their effect on brittle-ductile transition is examined. Debonding between particles is identified in DEM algorithm. Simulation results indicate that the proposed DEM with debonding mechanism is capable of replicating the brittle-ductile transition of frictional-cohesive materials. Furthermore, the simulations also reveal a consistent trend that links the development of microcracks with rapid changes of local couple stress. Close examinations of the specimen-scale and grain-scale couple stress indicate that the sudden increase of the local couple stress is an indicator for the onset of cataclastic flow.

This paper is organized in the following manner. Section 2 introduces the governing equations and constitutive laws used in the discrete element simulations. The constitutive law that replicates the compressive and tensile normal forces and the Mohr-Coulomb-type frictional model for tangential force are described. Section 3 describes how to setup the biaxial simulations and presents the results obtained from the DEM simulations. Section 4 further analyzes the numerical simulations and compares them with previous published experimental and numerical data. The new contribution is then summarized in section 5.

2. DEM Model for Bonded Cohesive-Frictional Materials

Previous numerical studies on brittle-ductile transition have successfully developed macroscopic phenomenological models, in particular, cap plasticity models, to replicate the brittle-ductile behavior at the continuum scale [Sun *et al.*, 2014; Lyakhovskiy *et al.*, 2015]. Nevertheless, since the brittle-ductile transition is originated from a combination of microstructural deformation mechanisms of discrete natures (e.g., crushing and rolling of particles), discrete models, such as the lattice spring model [Katsman *et al.*, 2005] and the discrete element method [Cundall and Strack, 1979], may shed light on connecting the macroscopic mechanical responses to the microstructural origins.

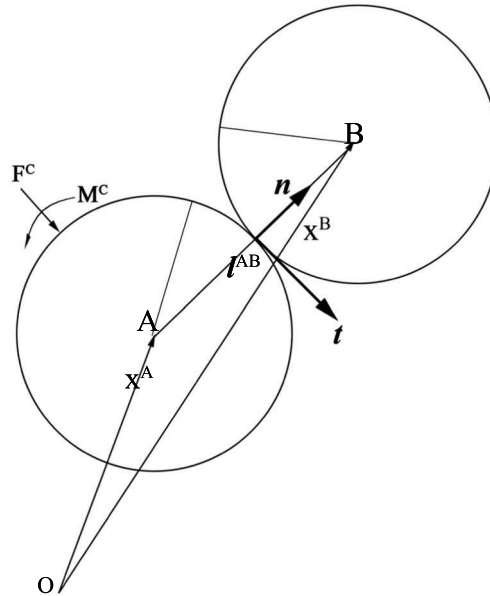


Figure 1. Contact model between particle pair AB with moment resistance, bonding/debonding mechanism, and frictional contact.

DEM has been used to simulate the behavior of frictional-cohesive materials ever since it was proposed [Cundall and Strack, 1979; Camborde et al., 2000; Delenne et al., 2004]. In DEM model, particles or grains retain their shapes and sizes but may be interpenetrated.

To replicate both the cohesive and frictional behaviors during the brittle-ductile transition, we employ a discrete element model with contact law that takes account of the internal force and moment triggered by normal compression, sliding, rolling, and bonding among particles. A point of departure is the introduction of softening and debonding state upon reaching a failure criterion. This mechanism enables one to capture the loss of strength due to the microscopic damage accumulated at the grain contact. The details of the softening and debonding models will be discussed in the next section.

Furthermore, it is important to point out that the current model does not explicitly incorporate any grain crushing mechanisms showcased in Wang et al. [2008] and Marketos and Bolton [2009]. As shown in the next few sections, this limitation does not prevent the onset of brittle-to-ductile transition but may make it difficult, if not impossible, to trigger the propagation of compaction band. Incorporating a realistic model that can sufficiently capture the essence of grain crushing is an important task that is currently undertaken by the research team but is out of the scope of this study.

2.1. Normal and Tangential Forces

In the proposed DEM model, the normal force $\vec{F}_n = F_n \vec{n}$ may exert on the contact of two particles orthogonal to normal vector \vec{n} and/or introduced via bonding between particles that are close but not necessarily in contact. As a result, normal force \vec{F}_n acting in-between particles is split into compressive-contact and tensile-bonding components. Both components are captured by a constitutive law, which can be conceptually simplified as a spring (with different compressive and tensile stiffness) linking the particles [Tavarez and Plesha, 2007]. The magnitude and sign of the force are then related to overlap or separate between two interacting particles as shown in Figure 1, which can be expressed in the incremental form as

$$\Delta F^n = k_n \Delta \delta_n, \quad \Delta \delta_n = \Delta l_i^{AB} \cdot n_i^{AB} \quad (1)$$

when there is no debonding between two particles (e.g., $\|l^{AB}\| \leq (r_A + r_B)$), where \vec{l}^{AB} represents the branch vector between the contacted particles, the product δ_n is the magnitude of increment of the branch vector in normal direction, r_A and r_B are radius of particles. The symbol Δ denotes the change between two incremental loading steps.

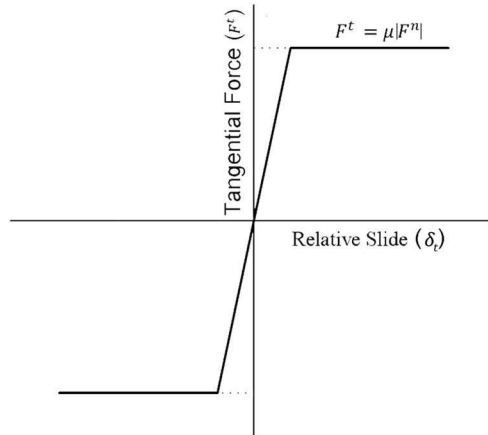


Figure 2. Property of tangential contact force with frictional condition.

The tangential force, F^t , is defined in the similar incremental form of which the change of the tangential force ΔF^t is a function of the change of the relative slip δ_t unless the Mohr-Coulomb criterion is met, i.e.,

$$F^t \leq C + F^n \tan \phi \quad (2)$$

where ϕ represents fictional angle of contact interface, C is the cohesion. The resultant governing equation for tangential force (as illustrated in Figure 2), therefore, reads

$$\Delta F^t = k_t \Delta \delta_t, \quad \Delta \delta_t = \Delta l_i^{AB} \cdot t_i^{AB} \quad \text{if } F^t \leq C + F^n \tan \phi \quad (3)$$

$$F^t = \mu F^n \quad \text{if } F^t = C + F^n \tan \phi \quad (4)$$

where superscript t indicates the tangential direction and t_i^{AB} are the component of the unit vector in tangential direction of the grain contract between grains A and B. For geomaterials which are known to be cohesive-frictional, grains may be cemented or bonded together before the bonds break. As a result, the micromechanical model must be able to replicate the tensile strength exhibited in real specimen. In the proposed mode, grain-to-grain force in the normal direction can be either compressive contact force or the tensile bonding force. However, the two types of force do not coexist in the same grain pair. Two bonding models are introduced to describe the relationship between tensile force and the particle separation. The first one, which is referred to as DEM model I herein, is a bilinear softening model. This tensile force displacement model is a variant of the elastoplastic spring model. During the initial loading, the tensile stiffness of the grain pair is constant until the tensile force reaches the initial critical value $f(F^n) = F^n - F_m = 0$. Upon reaching the critical value, the damage of the bonding accumulates if the loading continues and a negative softening modulus $-k_{sf}$ is introduced to replicate this damage process such that,

$$\Delta F^n = \begin{cases} k_n \Delta \delta_n & \text{(elastic branch)} \\ (-k_{sf} k_n) \Delta \delta_n / (-k_{sf} + k_n) & \text{(softening branch)} \end{cases} \quad (5)$$

If unloading occurs, then the tensile stiffness that governs the increment changes of force and displacement is identical to elastic branch counterpart (shown in Figure 3, left). To replicate the path-dependent behavior, a scalar internal variable α is introduced such that the following isotropic flow rule applies, i.e.,

$$\Delta \alpha = \Delta \delta_n^p \quad (6)$$

where δ_n^p is the irreversible relative displacement, i.e., $\delta_n^p = \delta_n - \delta_n^e$, and the symbol Δ denotes the change between two incremental loading steps. As a result, the tensile force is evolved via the following constraints

$$f(F^n, \alpha) = F^n - F_m + k_{sf} \alpha \leq 0 \quad \text{(Strength criteria)} \quad (7)$$

$$\Delta \alpha \geq 0, \quad f(F^n, \alpha) \leq 0, \quad \Delta \alpha f(F^n, \alpha) = 0 \quad \text{(Kuhn-Tucker condition)} \quad (8)$$

$$\Delta \alpha \Delta f(F^n, \alpha) = 0 \quad \text{(Consistency condition)} \quad (9)$$

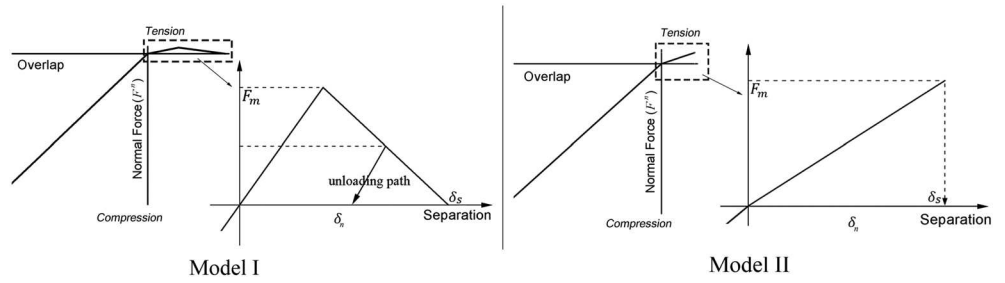


Figure 3. Constitutive models of contact/bonding force which describe the relationship between normal force and relative translation (overlap or separation). (left) The cohesive bonding force model and (right) the brittle bonding force model.

An alternative simplified debonding model, which we refer to as DEM model II, replicates a brittle process in which the contact force drops directly to zero when the tensile force F^n reaches the critical value (as shown in Figure 3, right). Both models are adopted in this work, the DEM model I is regarded to be suitable in discrete modeling of quasi-brittle materials [Kim et al., 2008] or frictional-cohesive materials [Luding, 2008], while the DEM model II has been used to model the brittle failure of granular materials [Jiang et al., 2005].

The two tensile bonding force models are both implemented in DEM code OVAL [Kuhn, 2011]. Bonding breakages are identified by a modified detection algorithm that excludes the debonded particle pairs. Explicit algorithm is applied to compute the displacement and spin from particle to particle by summing up the forces and moments applied by interior neighborhood particles or exterior boundary condition.

2.2. Rolling Resistance and Moment

Rolling resistance which rises from relative rotation may influence the responses of DEM assemblies, such as peak strength, dilatancy, and internal friction by preventing particles from rolling freely. The rolling resistance contact law may also affect the couple stress, which is a function of both tangential force, moment, and branch vector of each particular contact [Chang and Ma, 1990; Bardet, 1994; Oda and Iwashita, 2000; Lanier, 2001]. The rigid body motion of particles in DEM can be divided into the rolling (or rotation) part and the sliding part [Iwashita and Oda, 1998]. Rolling resistance model relates the internal moment M^c and the incremental relative rotation $\Delta\delta_\theta$ with respect to particle A in a single contact by resistance stiffness k_θ

$$\Delta M^c = k_\theta \Delta \delta_\theta \tag{10}$$

Physically, the rolling resistance moment is caused by unevenly distributed traction on contact interface and is related to the particle shapes. It is regarded to be significant when particles have strong self-spin, but there is no established method to identify the exact value of rolling resistance. As a result, one way is to follow the approach in Jiang et al. [2005] which relates the rolling stiffness k_θ with the branch vector and the normal or tangential stiffness of contact force. A linear distribution of traction on contact interface is assumed and then the rotation stiffness related to normal contact force reads,

$$k_\theta = \frac{k_n (\lambda B)^2}{12} \tag{11}$$

where B is the width of contact interface, which can be calculated based on particle positions in DEM simulation. λ is a parameter related to particle shape, which ranges between 0.1 and 1.6 and is selected as 1 here because of the circular shape of particles. Similar to the bonding force, there is a strength limit for the resistance moment M_m and a breaking value for relative rotation Θ_s . The constitutive model is in the form as shown in Figure 4.

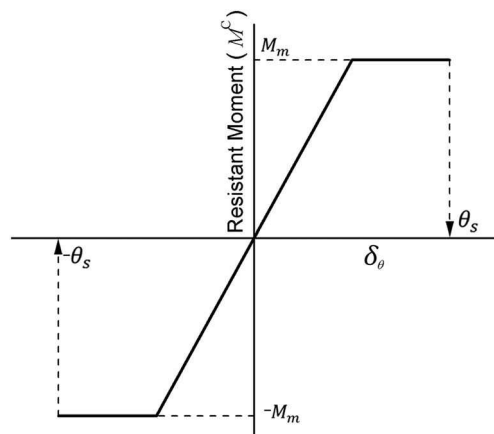


Figure 4. Constitutive model of rolling resistance moment with relative rotation.

Once the breaking criterion is met, the rolling resistance is permanently lost and the relative rotation

Table 1. Constitutive Model of Contact Force, Bonding Force, and Rolling Resistance Moment for Model I and Model II

	Model I	Model II
Contact force	tangential force: Mohr-Coulomb friction model normal force: linear model	
Bonding force	bilinear softening cohesive	brittle
Rolling resistance moment	elastic-perfectly plastic model with a strength limit	none

becomes free. Meanwhile, the rolling resistance also depends on bonding/contact behavior of particles such that the resistance moment would vanish when particles are actually bonded but not in contact; i.e., $k_\theta = 0$ when $\|I^{AB}\| \geq (r_A + r_B)$. The normal force, tangential force, and resistance moment are related with bonding force, friction, and debonding.

The rolling resistance is included in Model I with cohesive bond for the modeling of frictional-cohesive material. Constitutive models of force and moment are listed in Table 1 for Model I and Model II, respectively.

Parameters used in the DEM computation with bonding force and rolling resistance can be calibrated against available experimental data [Kazerani and Zhao, 2010] under room temperature. Here Adamswiller sandstone is taken as a representative porous material in the analysis; normal and tangential contact stiffness (k_n and k_s) are calibrated according to Young's modulus of 5 GPa and Poisson ratio of 0.3; tensile stiffness is approximated to be 1/5 to the compression stiffness. Tensile strength (F_m) and separation limit (Δ_s) of bond is determined with respect to a tensile strength of 4 MPa and a strain limit of 10%. The parameters after calibration are listed in Table 2.

2.3. Calculation of Couple Stress

Classical Boltzmann continuum does not possess any intrinsic material length scale. Constitutive responses of Boltzmann continua are therefore regarded as a relation among the stress, strain, and internal variables of a material point. This treatment is sufficient in many situations where the Boltzmann continuum assumption is valid. However, materials that contain defects, such as notches, holes, and cracks are not suitable to be idealized as first-order continua. In that case, higher-order theory that considers length scale and microstructures may provide new insights on the deformation processes. Since the brittle-ductile transition of rock is often related to the grain-crushing followed by sliding and rolling of fragments within the cataclastic rock, it is important to analyze stress related to nonhomogeneous straining and strain gradient. To address this issue, Cosserat Continuum Mechanics is adopted to analyze with the high-order continuum effect originated from the defects of microstructure.

The local couple or micropolar stress μ_{ij} , the torque per unit area acting on individual particle P reads [Chang and Ma, 1990],

$$\mu_{ij}^p = \frac{1}{V} \sum_c \left(m_j^c + e_{jkl} f_k^c r_l^c \right) (x_i^a - x_i^b) \quad (12)$$

where m_i is the rolling resistance torque, r_i^c is the radius of the particles in contact with the particle P, superscript c represents contact particle, and x_i^c and x_i^p are the centroid positions of particles.

Table 2. Calibrated Material Parameter for DEM Simulation

Parameter	Particulars	Values
k_n^1	stiffness of normal compress contact	1.9×10^8 N/m
k_n^2	stiffness of normal tensile bonding	4×10^7 N/m
k_t/k_n^1	ratio between tangential and normal contact stiffness	0.62
k_{sf}	softening stiffness of contact	1×10^7 N/m
μ	friction coefficient	0.61
F_m	tensile strength of normal force	180 N
δ_s	limit separation of cohesive force	1.8×10^{-2} mm

In order to analyze the micropolar effect on the macroscopic responses during the brittle-ductile transition, we adopt the concept of macroscopic couple stress to measure micropolar effect for the global specimen assembly. *Oda and Iwashita* [2000] define the macroscopic couple stress as the average of couple stresses along a plane. Another definition is suggested by *Bardet and Vardoulakis* [2001]. Based on virtual work principle and an expansion of displacement field up to the second order strain gradient, macroscopic couple stress can be expressed as

$$\mu_{ij}^c = \frac{1}{V} \sum_c \left(e_{jkl} f_l^c (x_i^b (x_k^c - x_k^b) - x_i^a (x_k^c - x_k^a)) + m_j^c f_i^c \right) \quad (13)$$

This expression is also referred to as the transported couple stress—a combination of first-order moment caused by contact force and torque. *Chang and Kuhn* [2005] give a similar expression based on a different expansion of displacement field, which reads,

$$\mu_{ij}^c = \frac{1}{V} \sum_c \left(e_{jkl} f_l^c \left(x_i^b (x_k^c - 1/2 x_k^b) - x_i^a \left(x_k^c - \frac{1}{2} x_k^a \right) \right) + m_j^c f_i^c \right) \quad (14)$$

The definitions of macroscopic couple stress by *Bardet and Vardoulakis* [2001] and *Chang and Kuhn* [2005] are both based on higher-order constitutive relationship; however, the expressions mentioned above are not purely contributed from couple stress. In order to focus on the couple stress in a macroscopic view a simplified averaging concept is considered and an averaged couple stress is adopted here as

$$\bar{\mu}_{ij} = \frac{1}{V_s} \sum_p \mu_{ij}^p V^p \quad (15)$$

where V_s is overall volume of the solid particles, V^p is bulk of one particle in the system. The volume degenerates to area in two-dimension problems. This definition is similar to the previous studies and is easy to be measured.

According to *Oda and Iwashita* [2000] and *Alshibli et al.* [2006], couple stress is significant in indicating the formation of strain localization and cataclastic flow, where there is high gradient of rotation rate at boundaries of band or fragment. In fact, since the couple stress is related to the torque and moment introduced by particle interactions, the connection between the couple stress and the relative motion among particles during the brittle-ductile transition can be established. In particular, the invariant of the couple stress can be related to microscopic damages, because the damages represented by the debonding of contact at DEM may enhance particle rotation and hence by investigating the couple stress, some parts of brittle-ductile transition mechanism rises from the grain scale can be analyzed. It should be noticed that couple stress here is used as a measurement of the micropolar effect, but the natural and essential boundary conditions we imposed on the boundary of the DEM assemblies are only of first order (i.e., either traction or displacement is applied at the boundaries).

3. Problem Setup and Results

3.1. Numerical Simulation Setup

A two-dimensional DEM numerical specimen consisting of 4000 circular disks as illustrated in Figure 5 is used in this study. The initial 2-D porosity of the numerical specimen before being subjected to isotropic compression is 22.6%. As indicated by a previous 2-D DEM study by *Wang et al.* [2008], using 2-D assemblies composed of idealized circular disks allows one to easily introduce spatial heterogeneity and incorporate microstructural attributes, such as grain size distribution, into the numerical simulations. Nevertheless, the 2-D DEM model also oversimplifies the geometrical attributes and topology of the force chain. We will seek improvement on numerical methods in the future study but the extension to 3-D particulate assemblies composed of particles with realistic shapes is out of the scope of this study.

In this study, we generate a numerical specimen with the same grain size distribution of the Adamswiller sandstone. As a result, the 2-D disks have radius ranging from 0.052 mm to 0.13 mm and the average radius is 0.092 mm. The material parameters used to replicate the contact indentation, tensile bonding, frictional sliding, rolling resistance, and bonding breakage with the DEM models I and II are summarized in Table 1.

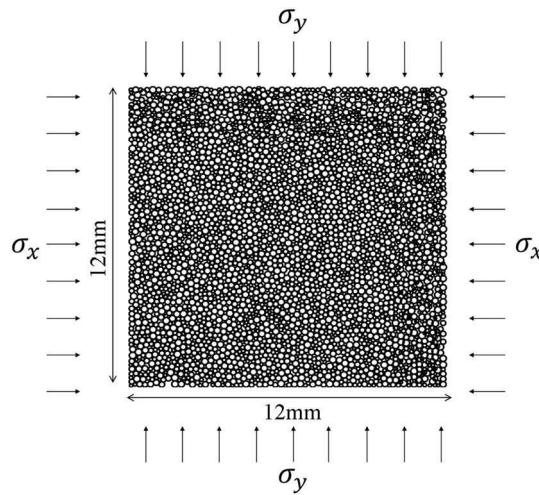


Figure 5. DEM model of a sandstone with dimension of 12 mm × 12 mm and constituted by 4000 circular particles, which is subjected to biaxial compaction test with loading along the y direction.

These material parameters were calibrated with the Adamswiller sandstone data set. However, due to the aforementioned limitations stemmed from the 2-D model and the idealized circular shape of the 2-D disks, our objective is limited at obtaining a trend qualitatively consistent with the brittle-ductile transition observed in the experimental studies in *Wong et al.* [1997], rather than finding the optimal material parameters that provide the best curve fitting as done in *Liu et al.* [2015]. Simulations of biaxial two-dimensional compaction tests under confining pressure of 5 MPa, 20 MPa, 40 MPa, 60 MPa, 100 MPa, and 350 MPa are conducted in two phases. First, a hydrostatic load is incrementally increased until the desired confinement is reached. Following the isotropic compression, vertical displacement (displacement in y direction) is prescribed on the top and the bottom layers of the specimen to replicate a drained biaxial compression.

3.2. Brittle-Ductile Transition

For DEM Model I, the evolution of differential stress ($\sigma_1 - \sigma_3$) (which is applied to evaluate shear degree) with axial strain under different confinements are shown in Figure 6 (left). The shift trend of the curves is

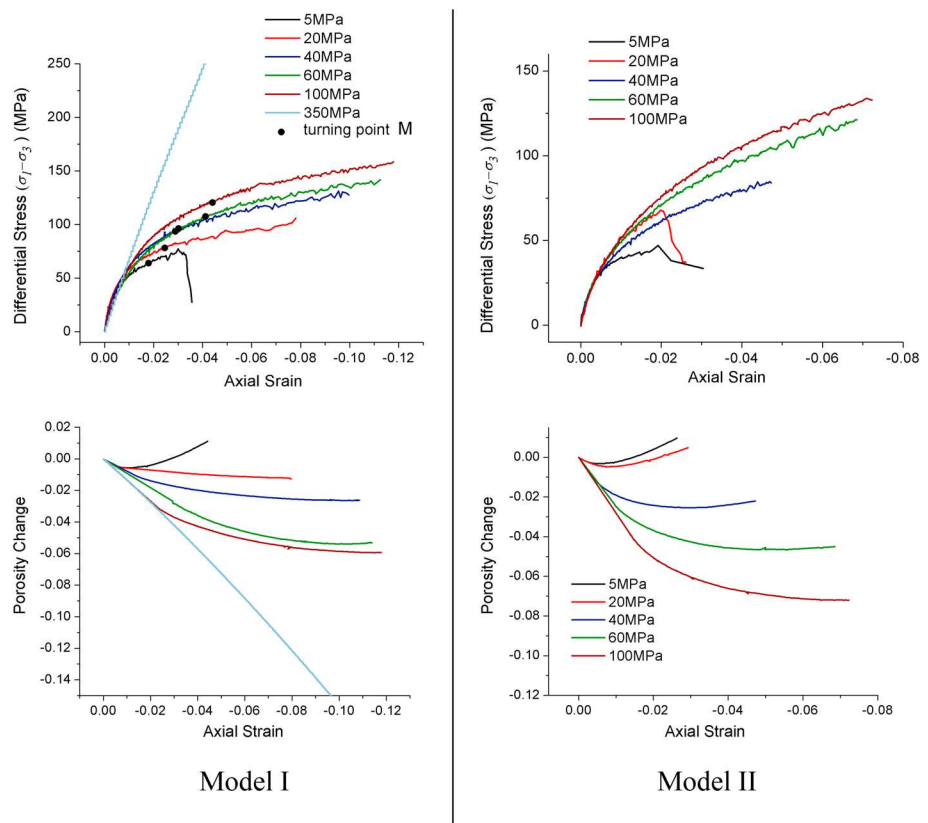


Figure 6. Shift of evolution of differential stress and porosity change with axial strain with respect to different confinements, calculated with (left) Model I considering rolling resistance and cohesive bond and (right) Model II considering free relative rotation and brittle bonding. The turning point M is marked for significant change in evolution micropolar effect. Initial porosity is 22.6%.

qualitatively consistent with the brittle-ductile transition trend in the experimental work by *Wong et al.* [1997] for the study of brittle-ductile transition of Adamswiller sandstone. Such a transition is also observed in other sandstones, such as Darley-Dale sandstone [*Wong et al.*, 1997], Boise sandstone [*Wong et al.*, 1997; *Cheung et al.*, 2012], Berea sandstone [*Menéndez et al.*, 1996], and Bentheim sandstone [*Klein et al.*, 2001]. A summary of the experimental work on various types of sandstones can be found in Table 1 of *Wong and Baud* [2012]. Peak differential stress increases with confinement significantly; the peak stress under confinement of 150 MPa is about 2 times the peak stress under confinement of 5 MPa. Differences in response are also observed in the change of porosity which is also illustrated in Figure 6, where dilatancy is only observed in the case under confinement of 5 MPa.

When the specimen is under relatively low confinement (5 MPa), brittle failure is observed. As the strain increases, the differential stress begins a rapid decrease after researching the peak value (77 MPa), which indicates a sudden drop of load-carrying capacity. The dilatancy of the specimen after the initial contraction found in the simulations are also consistent with what should have happened in the brittle failure regime.

When confinement is higher (20 MPa or higher), a different pattern of differential stress evolution is obtained with hardening. A turning point M is marked which is slightly after yielding point for the discussion of micropolar effect in the following section. The specimen can still deform stably without rising differential stress level for a long period after peak and sustain to carry load, which is a ductile feature. The porosity continues decreasing till the end, showing that compaction runs through the numerical test.

The differential stress against axial strain obtained from Model II is plotted in Figure 6 (right) with different confinements from 5 MPa to 100 MPa. The strength and stiffness of the specimen are lower compared to the results obtained with Model I. Take the case under confinement of 60 MPa, for example, the peak stress is lowered by 14.6% and the strain at failure is lowered by 39.2%. It is quite obvious since the resistance to external loading is decreased due to the absence of rolling resistance and cohesive bond in Model II.

The evolution processes of differential stress still exhibit similar feature. The shift of failure pattern from brittle to ductile is also demonstrated as the confinement increases. However, comparing the results obtained with DEM Model I and Model II under confinement of 20 MPa, the evolution of differential stress obtained with Model I exhibits characteristics of ductile failure that no decrease is observed after peak. In contrast, the result obtained with Model II is more brittle that the peak stress is lower and the constitutive response is similar to that in brittle regime (under confinement of 5 MPa), a drop or softening behavior is captured after peak stress.

3.3. Cataclastic Flow Under High Confinement

In this section, we focus on the cataclastic flow observed at the high confining pressure. Initial porosity of numerical specimen is again relatively high to promote the onset of the cataclastic flow accompanied by compaction. The effect of shear on compaction in ductile regime (under confinement of 40 MPa, 60 MPa, and 100 MPa) can be viewed from the curve of effective mean stress $((\sigma_1 + 2\sigma_3)/3)$ with porosity reduction in Figure 7. The decreasing of porosity is more profound after the yielding and such a porosity change is caused by shear-enhanced compaction [*Cheung et al.*, 2012]. When confinement becomes higher and closer to a hydrostatic loading state, the shear effect is suppressed. This observation can be compared with experimental results reported by *Wong et al.* [1997] and *Klein et al.* [2001] as well as the numerical simulations in *Wang et al.* [2008].

The gradual shift of failure mode from brittle faulting to ductile cataclastic obtained with DEM simulation is plotted in Figure 8 under typical confinement of 5 MPa, 40 MPa, and 100 MPa. The microcracks in grain-scale are represented by debonding (red lines in the figure) between particles.

When the confinement is at 5 MPa, the distribution of debonding is highly concentrated in only one localized zone with high relative deformation gradient when axial strain is high. When the confinement rises to 40 MPa, the localization bands with microcracks may form in as a tabular structure; meanwhile, there is obviously an increase in the number of bond breakages. At the location where the localized bands coalesce, the debonding process among particles are much more profound. These debonded particles exhibit constitutive responses of a nonadhesive grains. At this stage, the original specimen is then cut into several fragments by the debonding bands. The failure pattern under confinements of 100 MPa is consistent with a cataclastic flow where a dominated localized zone is absent and the damage is more uniformly distributed. Debonding between particles is distributed throughout the specimen and there is no localization or

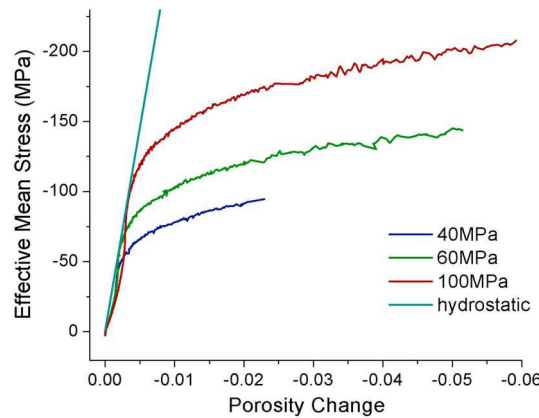


Figure 7. The curve of mean stress as a function of porosity in ductile regime, which illustrates the effect of shear on compaction.

concentration phenomenon. More microcracks can be observed in this cataclastic flow failure pattern, which can be referred to as high microcracking density [Menéndez et al., 1996].

3.4. Couple Stress

In the DEM simulations, couple stress of individual particles and that of the whole specimen are both computed to evaluate micropolar effect. Meanwhile, initiations of microcracks are monitored. Evolutions of the first invariant of averaged couple stress (referred to as averaged couple stress for short, which is expressed as equation (15)) in compression tests under confinement pressures from 5 MPa up to 350 MPa are shown in Figure 9 along with the number of particle debonding.

The averaged couple stress can be applied to evaluate the micropolar effect of the specimen. The first invariant of averaged couple stress at final failure under confinement of 40 MPa is about 4 times or more than that under

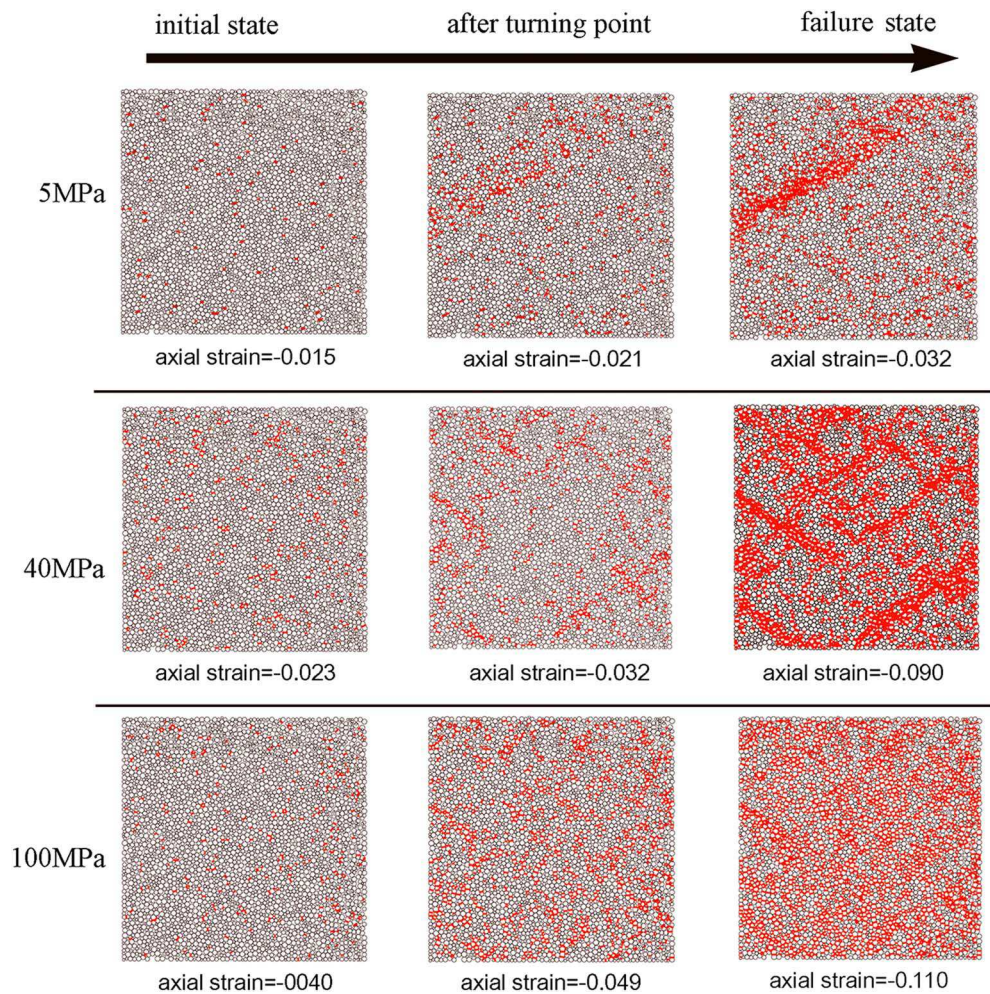


Figure 8. Evolution of microcracking distribution from initial loading to final failure stage under magnitude of confinement of 5 MPa, 40 MPa, and 100 MPa with microcracks represented by bond breakages between particles pairs (red lines). The failure pattern initially shows single deformation band (5 MPa), then shifts to multiple deformation bands (40 MPa), and finally cataclastic flow (100 MPa).

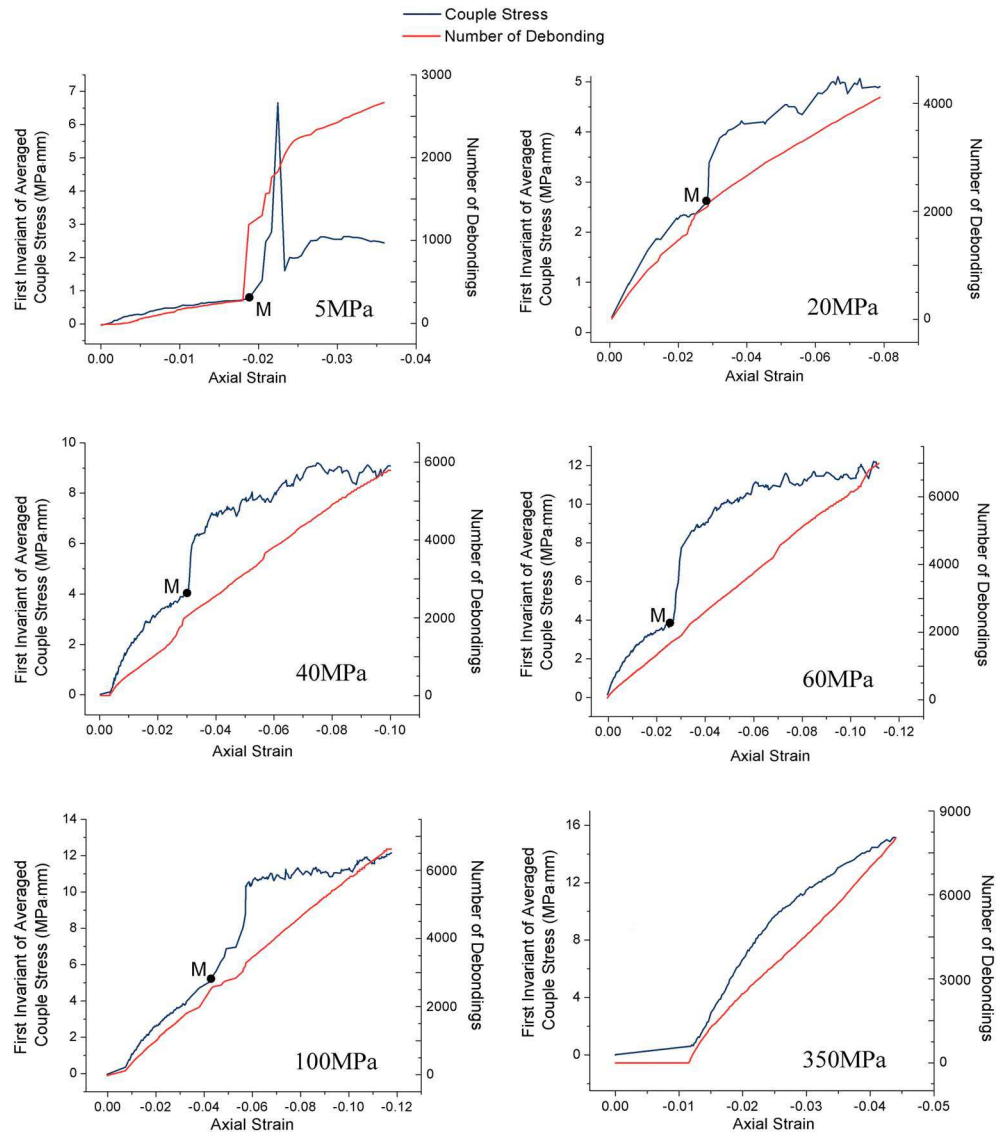


Figure 9. Evolution of the first invariant of averaged couple stress and number of debonded particle pairs with axial strain under different confinements (from 5 MPa to 350 MPa). The turning point M marks a rapid increase of the couple stress.

confinement of 5 MPa, which indicates higher micropolar effect in the ductile field. Whereas the peak values of averaged couple stress under higher confinements are relatively close and in same order of magnitude. The peak couple stress under confinement of 40 MPa is just 35.3% lower than that in the case under confinement of 350 MPa; in contrast, the confinement is 88.6% lower. Similarly there are more debonding particles in ductile regime.

The evolution process of averaged couple stress and debonding numbers shown in Figure 9 can be divided into several stages. In the initial loading stage, the average couple stays at a low level (before the point M in the figure) with increasing debonding particle pairs. When the compressive load increases to the turning point M which can be viewed as a critical point for the generation of micropolar effect, the couple stress value starts to increase rapidly, and the response shows that more fluctuate with small amplitude. While under higher confinements, the evolution of debonding number is stable after yielding, which indicates a relatively fixed debonding rate. The point M in the curve is actually slightly after the yielding point, which can be seen in the stress curve in Figure 6.

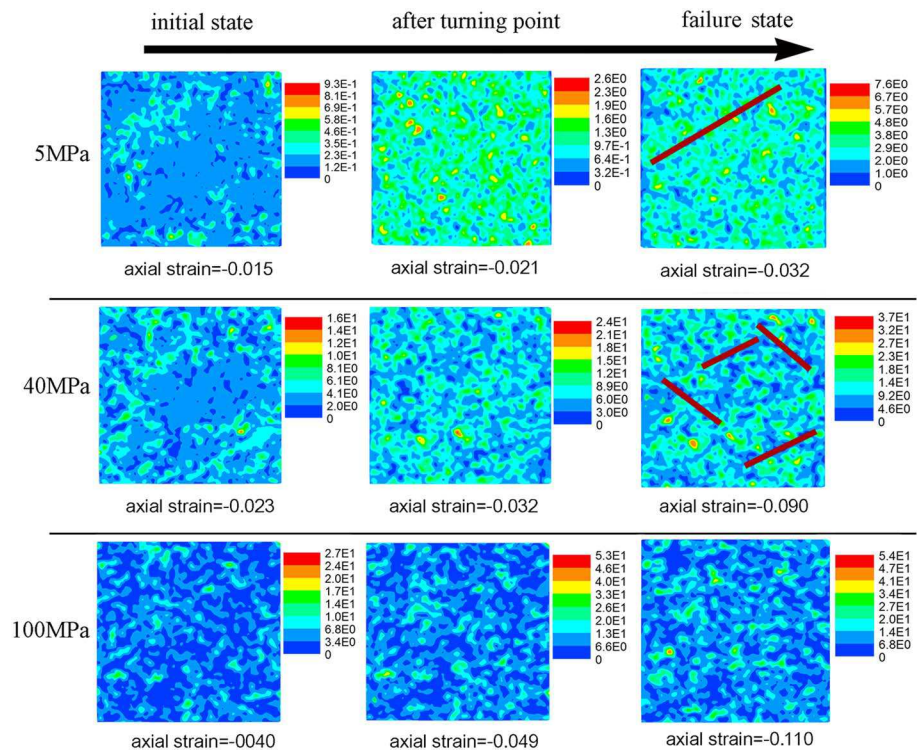


Figure 10. Successive evolution state of distribution of the first invariant of local couple stress (unit: MPa mm) from initial to final failure state under confinements of 5 MPa, 40 MPa, and 100 MPa. The debonding bands are marked by dark red bars.

In the final failure stage, the evolution of averaged couple stress enters a plateau phase. In the ductile regime, the increase of averaged couple stress is slowed down before failure and evolve with small amplitude of oscillation. Meanwhile, the number of debonded particle pairs continues to increase. This debonding stage is more apparent when confinement is higher than 40 MPa. However, this pattern of couples stress evolution is not observed in the case under confinement of 350 MPa. In the brittle regime under a confinement of 5 MPa, after reaching this final stage, the evolution of couple stress is minimal after peak. However, the debonding process accelerates after the turning point M.

Evolution of the couple stress distribution of the numerical specimen under different confinements are shown in Figure 10 where the first invariant of the couple stress is plotted. We select confinements of 5 MPa, 40 MPa, and 100 MPa to cover both brittle and ductile fields. This couple stress is computed in grain scale; it can show the local micropolar effect from initial to final failure stage. The distributions of couple stress could be related to the distribution of microcracks represented by particle debonding in Figure 8. The distribution of couple stress at failure shows a localized feature where the debonding bands and concentration of microcracks are located (especially under confinement of 40 MPa in the figure), while it becomes irregular and distributed at failure with cataclastic flow (under confinement of 100 MPa).

4. Discussion

4.1. Influence of Cohesive Bonding and Rolling Resistance

Cohesive bonding and rolling resistance are included in the DEM Model I. Using the DEM models without cohesive bonding, the previous works by *Iwashita and Oda* [1998], *Delenne et al.* [2004], and *D'Addetta et al.* [2002] were able to replicate the formation of deformation band numerically, while *Cheng et al.* [2003] observe obvious strain hardening upon yielding. These researches are often focused on specific deformation process at a limited range of confinement. The point of departure of this work is to explore the possibility of using a single DEM model to predict the responses in both the brittle and ductile regimes.

The results shown in Figure 6 indicate that a major difference between the results obtained with DEM Model I and Model II is the transition pressure. It can be inferred that the confinement pressure of 5 MPa and 20 MPa

can be viewed as the lower and upper bounds of the transition pressure for the DEM Model I, while for the DEM Model II, the lower and upper bounds of transition pressure are, respectively, 20 MPa and 40 MPa. Meanwhile, comparing the porosity change obtained via Models I and II, dilatancy caused by microcracking is more significant than that of Model I. Even under relative high confinement (40 MPa and 60 MPa) such a dilatancy still exists even though it is suppressed with the rising confining pressure.

Compared to the experimental and numerical tests data obtained for sandstone with relative high initial porosity (about 20%) [Menéndez *et al.*, 1996; Wong, 1990; Wong *et al.*, 1997; Klein *et al.*, 2001], especially the data reported by Wong *et al.* [1997] for Adamswiller sandstone, dilatancy and stress evolution with brittle failure are absent with confinement more than 20 MPa during the transition process. As a result, one may argue that DEM Model I is more consistent with the experimental observation in a phenomenological sense. Therefore, our focus is on the micropolar effect and cataclastic flow observed from the DEM Model I.

The lower transition pressure with DEM Model I indicates that when rolling resistance and cohesive bond are included in interparticle property, ductile property of the porous material is enhanced and results in a lower brittle-ductile transition confining pressure. In macroscopic view, less dilatancy in the simulation with rolling resistance and cohesive bonding indicates that the resistance moment and cohesive tensile force suppress the occurrence of shear, while shear is an important cause of dilatancy for the porous material.

In contrast, as the confinement increases, pore collapse and grain crushing become more important [Wong and Baud, 2012] in the deformation process. The grain crushing in the DEM model can make cataclastic flow easier to happen, thus pushing the failure mode into ductile field at a lower transition pressure. It may also be viewed in grain scale that according to particle interactive mechanism, stronger strength caused by cohesive bonding force as well as rolling resistance makes the propagation of the main debonding band more difficult. As a consequence the growth and coalescence of microcracks become more stable [Nguyen *et al.*, 2001; Wong *et al.*, 2004], and more microcracks would appear and localized brittle faulting is prevented.

4.2. Role of Microcracking

In Figure 8, there are more microcracks in the ductile regime. The microcracking in grain scale is related to the path-dependent behavior including plastic yielding and damage [Wu *et al.*, 2000; Wong *et al.*, 1997; Wong and Baud, 2012; Lyakhovskiy *et al.*, 2015]. The microscopic intergranular constitutive model used in the DEM is significant to simulate pore collapse and grain crushing in compaction localization. The simulations reported in Wang *et al.* [2008] incorporating grain crushing model are able to replicate both the formation of compaction band and cataclastic flow. Li and Holt [2002] and Holt *et al.* [2008] adopt a different grain crushing model that involves particle clusters and found that compaction band can be obtained in simulations.

In the DEM model used in this study, the effect of grain crushing is modeled implicitly through a path-dependent constitutive law for grain particles that resemble a traction separation law. Cohesive bonding is applied to make the initiation of microcracks close to the physical model of cohesive-frictional material.

Compared to the reported results on compaction localization by experimental tests [Wong *et al.*, 1997; Olsson and Holcomb, 2000] and numerical simulations [Li and Holt, 2002; Amitrano, 2003; Wang *et al.*, 2008] in which the AE (Acoustic Emission) events are monitored, the distribution of microcracks in Figure 8 is more dispersed and irregular over the whole specimen domain when the specimen fails with cataclastic flow. The initiation of microcracks indicates that introducing cohesive bonding increases the tensile strength among contact until debonding occurs. Meanwhile, the rolling resistance can also provide additional shear and normal strength.

A further insight of the cataclastic flow and its micromechanics can be found by tracking the generation of microcracks in Figure 8. There are few debonded particles in the initial loading stage. After reaching the turning point M which is shown in Figure 6, massive debonded particle pairs begin to occur. The turning point is after the onset of yielding; this is also reported in the AE test [Olsson and Holcomb, 2000; Townend *et al.*, 2008] for compaction bands in compaction failure. In the brittle regime, the deformation band forms after the peak stress, which is as observed in experimental monitoring [Menéndez *et al.*, 1996]. There are more microcracks emerging in the cases under confinement of 40 MPa and 100 MPa which fall into ductile category, the observation of the onset of debonding belongs to a feature of cataclastic ductile performance.

As shown in Figure 6 a final failure point is reached at the end of a long hardening period. When subjected to a confinement of 100 MPa the limit strain at the final stage is 11.8% which is much larger than the rupture strain of 3.56% under a 5 MPa confinement. More fragments or microcracks and larger relative displacement

between these fragments can result in larger final failure strain [Paterson and Wong, 2005] in cataclastic flow. While in Figure 8, the observed relative displacement between fragments is not obvious, which may be inhibited by high stress level [Menéndez et al., 1996]. Hence, compared to particle friction, microcracking could be the main reason for inelastic strain.

4.3. Relationship Between Micropolar Effect and Microcracking

Previous theoretical studies on brittle faulting has related the faulting mechanism with the micropolar effect [Twiss and Unruh, 1998; Žalohar, 2012] through investigation of relative movement over macroscopic faults. In the case of cataclastic flow of which a single predominated macroscopic crack is absent, the link between the onset of cataclastic flow and micropolar effect is not well understood. In this study, our focus is on the connection between micropolar effect and the cataclastic flow.

The simulation results showcased in the previous section all indicate that the micropolar effect is minor at the initial state where damage of the specimen is not severe. In the midstage of the evolution process, the degree of micropolar effect experiences rapid growth after the turning point, which indicates a link between the onset of microcracks and the magnitude of the first invariant of the couple stress. In particular, the damage represented by the particle debonding model reduces the resistance of the relative rotation among particles and that in return leads to the increase and oscillation of the couple stress. As shown in Figure 6, the turning point M locates after the onset of shear-enhanced compaction [Wong et al., 1997; Klein et al., 2001] and the onset of grain crushing and pore collapse [Wong and Baud, 2012; Wang et al., 2008]. However, when the relative rotation rises to a high value, the particle pair may break. Due to the free rotation after the breakage of cohesive bonds [Menéndez et al., 1996], the increase of couple stress possibly leads to significant grain rotation and the micropolar kinematics become more significant.

In the numerical simulations, the first invariant of the local couple stress is relatively high in the vicinity of the debonding bands before the appearance of localized bands. However after the debonding, narrow zones with concentrated damage caused by the debonding begin to form the turning point M. The first invariant of the couple stress within these localized bands drops to a relatively low level compared to the host matrix.

In the brittle regime, a single dominated deformation band has been formed in the 2-D DEM model. The DEM simulation on shear band by Oda and Iwashita [2000] indicates that the area with highest micropolar effect is on the boundary of the band. The area with low magnitude in the first invariant of the couple stress is observed inside the deformation band at failure, as shown in Figure 10. After debonding of the highly tensed particles at the boundary of the deformation band, most of the micropolar effects are released, increasing the couple stress then slow down due to brittle failure. Therefore, the micropolar effect remains minor. The releasing of micropolar effect is more profound within these localized debonding bands.

In the ductile regime, the failure mode shows more cataclastic features with widely distributed microcracks (shown in Figure 8). The continuous initiations of debonding indicates that there are still plenty of particle pairs with high level of relative translation or rotation. Therefore, the enhancement of micropolar effect is sustained at grain scale, and such cataclastic flow leads to larger ductile capability. However, in the final stage the increase of micropolar slows down, while the number of debonding particles continues to grow. It is possible that there is more releasing of the micropolar effect than increasing.

With a uniformly distributed microcracks and cataclastic flow under 100 MPa confinement, regions with spots with the large first invariant of the couple stress are scattered over the specimen. Moreover, the first invariant of couple stress is generally larger in the ductile regime. It may be inferred that the relative rotation before debonding is intense though the relative translation among particles may be reduced by the higher confinement.

5. Conclusion

A DEM model with cohesive-tensile bond and rolling resistance moment is adopted to analyze the pressure-induced brittle-ductile transition phenomenon of Adamswiller sandstone which is a frictional-cohesive material. The cataclastic flow in ductile failure regime is especially focused. Bonding force in cohesive or brittle-fracture type and rolling resistance moment are implemented as additional attributes of interactive property between particles. Breakage of particles is identified in bonding detection algorithm. Micropolar effects characterized by couple stress is investigated in the transition phenomenon. The initiation of microcracks is represented by debonding between particles. The major conclusions of this study are summarized as follows:

1. The macroscopic features of brittle-ductile transition can be replicated in DEM simulations with properly defined contact model that includes bonding/contact force, rolling resistance moment, and debonding mechanism. When confinement is increased, the shift from brittle to ductile and porosity change from dilatancy to compaction can be reproduced numerically. These results are qualitatively consistent with experimental results despite the limitations of the rather simple ones used in this study.
2. DEM assemblies with cohesive tensile bonding force and rolling resistance moment possesses more resistance to microcrack initiation and shows more ductile performance and lower transition pressure compared to the DEM assemblies without tensile and moment resistance.
3. Macroscopic couple stress shows different features in brittle and ductile field. In the brittle regime, the first invariant of the couple stress is much lower. For both brittle and ductile regimes, the evolution of macroscopic couple stress can be divided into three stages: initially, it stays at a low level and begins to increase rapidly after a turning point which is after yielding in the midstage. Finally, the increasing of couple stress is slowed down when axial strain is high.
4. The breakages of the bonding pairs and formation of deformation band may cause local change of couple stress. The numerical result suggests that couple stress can be adopted as an indicator for the brittle-ductile transition.

Acknowledgments

This research is partially supported by the Earth Materials and Processes program at the U.S. Army Research Office under grant contracts W911NF-14-1-0658 and W911NF-15-1-0581, the Mechanics of Material program at National Science Foundation under grant contract CMMI-1462760, and Provost's Grants Program for Junior Faculty who Contribute to the Diversity Goals of the University at Columbia University. These supports are gratefully acknowledged. Zheyuan Zheng also acknowledges the funding from Graduate Innovation Project of Jiangsu Province (KYLX-0094) and Excellent Dissertation and Creative Talent Fund (CE02-1-26). In this study, all data are available on request at the following e-mail address: wsun@columbia.edu.

References

- Alshibli, K. A., I. M. Alsaleh, and G. Z. Voyiadjjs (2006), Modelling strain localization in granular materials using micropolar theory: Numerical implementation and verification, *Int. J. Numer. Anal. Methods Geomech.*, *30*(15), 1525–1544.
- Amitrano, D. (2003), Brittle-ductile transition and associated seismicity: Experimental and numerical studies and relationship with the b -value, *J. Geophys. Res.*, *108*(B1), 2044, doi:10.1029/2001JB000680.
- Bardet, J. (1994), Observations on the effects of particle rotations on the failure of idealized granular materials, *Mech. Mater.*, *18*(2), 159–182.
- Bardet, J., and I. Vardoulakis (2001), The asymmetry of stress in granular media, *Int. J. Solids Struct.*, *38*, 353–367.
- Baud, P., T. Reuschle, Y. Ji, C. S. N. Cheung, and T.-F. Wong (2015), Mechanical compaction and strain localization in Bleurswiller sandstone, *J. Geophys. Res. Solid Earth*, *120*, 6501–6522, doi:10.1002/2015JB012192.
- Borja, R. I., and A. Aydin (2004), Computational modeling of deformation bands in granular media. I. Geological and mathematical framework, *Comput. Meth. Appl. Mech. Eng.*, *193*, 2667–2698.
- Borja, R. I. (2007), Localized and diffuse bifurcations in porous rocks undergoing shear localization and cataclastic flow, in *Computational Plasticity*, edited by E. Oñate and R. Owen, pp. 37–53, Springer, Netherlands.
- Camborde, F., C. Mariotti, and F. Donzé (2000), Numerical study of rock and concrete behaviour by discrete element modelling, *Comput. Geotech.*, *27*(4), 225–247.
- Camones, L. A. M., E. do Amaral Vargas, R. P. de Figueiredo, and R. Q. Velloso (2013), Application of the discrete element method for modeling of rock crack propagation and coalescence in the step-path failure mechanism, *Eng. Geol.*, *153*, 80–94.
- Chang, C. S., and M. R. Kuhn (2005), On virtual work and stress in granular media, *Int. J. Solids Struct.*, *42*, 3773–3793.
- Chang, C. S., and L. Ma (1990), Modeling of discrete granulates as micropolar continua, *J. Eng. Mech.*, *116*, 2703–2721.
- Cheng, Y. P., Y. Nakata, and M. D. Bolton (2003), Discrete element simulation of crushable soil, *Geotechnique*, *53*(7), 633–641.
- Cheung, C. S. N., P. Baud, and T.-F. Wong (2012), Effect of grain size distribution on the development of compaction localization in porous sandstone, *Geophys. Res. Lett.*, *39*, L21302, doi:10.1029/2012GL053739.
- Cundall, P. A., and O. D. Strack (1979), A discrete numerical model for granular assemblies, *Geotechnique*, *29*(1), 47–65.
- D'Addetta, G., F. Kun, and E. Ramm (2002), On the application of a discrete model to the fracture process of cohesive granular materials, *Granular Matter*, *4*, 77–90.
- Delenne, J., M. S. El Youssoufi, F. Cherblanc, and J. Bénéat (2004), Mechanical behaviour and failure of cohesive granular materials, *Int. J. Numer. Anal. Methods Geomech.*, *28*, 1577–1594.
- Evans, B., J. T. Fredrich, and T.-F. Wong (1990), The brittle-ductile transition in rocks: Recent experimental and theoretical progress, in *The Brittle-Ductile Transition in Rocks*, *Geophys. Monogr. Ser.*, vol. 56, edited by A. G. Duba et al., pp. 1–20, AGU, Washington, D. C.
- Holt, R. M., L. Li, and D. J. Holcomb (2008), A qualitative comparison between discrete particle modeling and laboratory observations of compaction bands in porous rock, in *The 42nd US Rock Mechanics Symposium, San Francisco, Calif., 29 Jun.–2 Jul.*, ARMA 08–292, 6 pp.
- Horii, H., and S. Nemat-Nasser (1986), Brittle failure in compression: Splitting, faulting and brittle-ductile transition, *Philos. Trans. R. Soc. A*, *319*(1549), 337–374.
- Iwashita, K., and M. Oda (1998), Rolling resistance at contacts in simulation of shear band development by DEM, *J. Eng. Mech.*, *124*, 285–292.
- Issen, K. A., and J. W. Rudnicki (2000), Conditions for compaction bands in porous rock, *J. Geophys. Res.*, *105*(B9), 21,529–21,536.
- Jiang, M., H.-S. Yu, and D. Harris (2005), A novel discrete model for granular material incorporating rolling resistance, *Comput. Geotech.*, *32*(5), 340–357.
- Kazerani, T., and J. Zhao (2010), Micromechanical parameters in bonded particle method for modelling of brittle material failure, *Int. J. Numer. Anal. Methods Geomech.*, *34*, 1877–1895.
- Katsman, R., E. Aharonov, and H. Scher (2005), Numerical simulation of compaction bands in high-porosity sedimentary rock, *Mech. Mater.*, *37*(1), 143–162.
- Kim, H., M. P. Wagoner, and W. G. Buttler (2008), Simulation of fracture behavior in asphalt concrete using a heterogeneous cohesive zone discrete element model, *J. Mater. Civ. Eng.*, *20*(8), 552–563.
- Klein, E., P. Baud, T. Reuschlé, and T.-F. Wong (2001), Mechanical behaviour and failure mode of Bentheim sandstone under triaxial compression, *Phys. Chem. Earth Part A*, *26*, 21–25.
- Kuhn, M. R. (2011), Implementation of Jäger contact model for discrete element simulations, *Int. J. Numer. Methods Eng.*, *88*(1), 66–82.
- Kuhn, M. R., W. Sun, and Q. Wang (2015), Stress-induced anisotropy in granular materials: Fabric, stiffness, and permeability, *Acta Geotech.*, *10*(4), 399–419.
- Lanier, J. (2001), Micro-mechanisms of deformation in granular materials: Experiments and numerical results, in *Continuous and Discontinuous Modelling of Cohesive-Frictional Materials*, edited by P. A. Vermeer et al., pp. 63–172, Springer, Berlin.

- Li, L., and R. M. Holt (2002), Particle scale reservoir mechanics, *Oil Gas Sci. Tech.*, *57*(5), 525–538.
- Liu, Y., W. Sun, and J. Fish (2015), Determining material parameters for critical state plasticity models based on multilevel extended digital database, *J. Appl. Mech.*, *83*(1), 011003.
- Liu, Y., W. Sun, Z. Yuan, and J. Fish (2015), A nonlocal multiscale discrete-continuum model for predicting mechanical behavior of granular materials, *Int. J. Numer. Methods Eng.*, doi:10.1002/nme.5139.
- Luding, S. (2008), Cohesive, frictional powders: Contact models for tension, *Granular Matter*, *10*(4), 235–246.
- Lyakhovskiy, V., W. Zhu, and E. Shalev (2015), Visco-poroelastic damage model for brittle-ductile failure of porous rocks, *J. Geophys. Res. Solid Earth*, *120*, 2179–2199, doi:10.1002/2014JB011805.
- Marketos, G., and M. Bolton (2009), Compaction bands simulated in discrete element models, *J. Struct. Geol.*, *31*, 479–490.
- Menéndez, B., W. Zhu, and T.-F. Wong (1996), Micromechanics of brittle faulting and cataclastic flow in Berea sandstone, *J. Struct. Geol.*, *18*(1), 1–16.
- Mogi, K. (1966), Pressure dependence of rock strength and transition from brittle fracture to ductile flow, *Bull. Earthquake Res. Inst. Univ. Tokyo*, *7*(25), 215–232.
- Nguyen, O., EA Repetto, M. Ortiz, and RA Radovitzky (2001), A cohesive model of fatigue crack growth, *Int. J. Fract.*, *110*(4), 351–369.
- Nygård, R., M. Gutierrez, R. K. Bratli, and K. Høeg (2006), Brittle-ductile transition, shear failure and leakage in shales and mudrocks, *Mar. Pet. Geol.*, *23*(2), 201–212.
- Oda, M., and K. Iwashita (2000), Study on couple stress and shear band development in granular media based on numerical simulation analyses, *Int. J. Eng. Sci.*, *38*, 1713–1740.
- Olsson, W., and D. Holcomb (2000), Compaction localization in porous rock, *Geophys. Res. Lett.*, *27*, 3537–3540.
- Paterson, M. S., and T.-F. Wong (2005), *Experimental Rock Deformation—The Brittle Field*, Springer, Berlin.
- Rudnicki, J. W., and J. R. Rice (1975), Conditions for the localization of deformation in pressure-sensitive dilatant materials, *J. Mech. Phys. Solids*, *23*, 371–394.
- Schöpfer, M. P., C. Childs, and T. Manzocchi (2013), Three-dimensional failure envelopes and the brittle-ductile transition, *J. Geophys. Res. Solid Earth*, *118*, 1378–1392, doi:10.1002/jgrb.50081.
- Smith, R. B., and R. L. Bruhn (1984), Intraplate extensional tectonics of the Eastern basin-Range: Inferences on structural style from seismic reflection data, regional tectonics, and thermal-mechanical models of brittle-ductile deformation, *J. Geophys. Res.*, *89*, 5733–5762.
- Sun, W. (2013), A unified method to predict diffuse and localized instabilities in sands, *Geomech. Geoen.*, *8*(2), 65–75.
- Sun, W., M. R. Kuhn, and J. W. Rudnicki (2013), A multiscale DEM-LBM analysis on permeability evolutions inside a dilatant shear band, *Acta Geotech.*, *8*(5), 465–480.
- Sun, W., Q. Chen, and J. T. Ostien (2014), Modeling the hydro-mechanical responses of strip and circular punch loadings on water-saturated collapsible geomaterials, *Acta Geotech.*, *9*(5), 903–934.
- Tavarez, F. A., and M. E. Plesha (2007), Discrete element method for modelling solid and particulate materials, *Int. J. Numer. Methods Eng.*, *70*(4), 379–404.
- Townend, E., B. D. Thompson, M. B. Philip, G. M. Philip, P. Baud, and R. P. Young (2008), Imaging compaction band propagation in Diemelstadt sandstone using acoustic emission locations, *Geophys. Res. Lett.*, *35*, L15301, doi:10.1029/2008GL034723.
- Tullis, J., and R. A. Yund (1980), Hydrolytic weakening of experimentally deformed Westerly granite and Hale albite rock, *J. Struct. Geol.*, *2*, 439–451.
- Twiss, R. J., and J. R. Unruh (1998), Analysis of fault slip inversions: Do they constrain stress or strain rate?, *J. Geophys. Res.*, *103*, 12,205–12,222.
- Wang, B., Y. Chen, and T.-F. Wong (2008), A discrete element model for the development of compaction localization in granular rock, *J. Geophys. Res.*, *113*, B03202, doi:10.1029/2006JB004501.
- Wong, T.-F. (1990), Mechanical compaction and the brittle-ductile transition in porous sandstones, *Spec. Publ. Geol. Soc. London*, *54*, 111–122.
- Wong, T.-F., and P. Baud (2012), The brittle-ductile transition in porous rock: A review, *J. Struct. Geol.*, *44*, 25–53.
- Wong, T.-F., C. David, and W. Zhu (1997), The transition from brittle faulting to cataclastic flow in porous sandstones: Mechanical deformation, *J. Geophys. Res.*, *102*, 3009–3025.
- Wong, T.-F., C. David, and B. Menendez (2004), Mechanical compaction, in *Mechanics of Fluid-Saturated Rocks*, edited by Y. Guéguen and M. Boutéca, pp. 55–114, Elsevier Acad. Press, Amsterdam.
- Wu, X. Y., P. Baud, and T.-F. Wong (2000), Micromechanics of compressive failure and spatial evolution of anisotropic damage in Darley Dale sandstone, *Int. J. Rock Mech. Min. Sci.*, *37*, 143–160.
- Žalohar, J. (2012), Cosserat analysis of interactions between intersecting faults; the wedge faulting, *J. Struct. Geol.*, *37*, 105–123.
- Zhang, X.-P., and L. N. Y. Wong (2013), Crack initiation, propagation and coalescence in rock-like material containing two flaws: A numerical study based on bonded-particle model approach, *Rock Mech. Rock Eng.*, *46*, 1001–1021.
- Zhu, W., P. Baud, and T.-F. Wong (2010), Micromechanics of cataclastic pore collapse in limestone, *J. Geophys. Res.*, *115*, B04405, doi:10.1029/2009JB006610.